Optical properties across the insulator to metal transitions in vanadium oxide compounds

TOPICAL REVIEW

Optical properties across the insulator to metal transitions in vanadium oxide compounds

A Perucchi[1], L Baldassarre[1], P Postorino[2] and S Lupi[2]

[1] Sincrotrone Trieste S.C.p.A., Area Science Park, I-34012 Basovizza, Trieste, Italy
[2] CNR-INFM Coherentia and Dipartimento di Fisica, Università di Roma 'La Sapienza',
Piazzale Aldo Moro 2, I-00185 Roma, Italy

E-mail: andrea.perucchi@elettra.trieste.it

Abstract
We review the optical properties of three vanadium oxide compounds V_2O_3, VO_2 and V_3O_5, belonging to the so-called Magnéli phase. Their electrodynamics across a metal to insulator transition is investigated as a function of both temperature and pressure. We analyse thoroughly the optical results, with a special emphasis on the infrared spectral weight. This allows us to discuss the nature of the mechanisms driving the phase transitions in the three compounds, pointing out the role of electron–electron and electron–phonon interactions in the various cases.

(Some figures in this article are in colour only in the electronic version)

Contents

1. Introduction

The understanding of the metal to insulator transition (MIT) in semiconductors thanks to the band theory of solids represented one of the most important achievements of the past century in condensed matter physics. The technical possibility to control the MIT enabled an unprecedented technological revolution, with *solid state* devices entering everyone's everyday life. The band theory, developed mainly by Bloch and Bethe [1, 2], explains the transport properties of matter in terms of completely filled or partially filled electronic bands.

As pointed out by de Boer and Verwey already in 1937, band theory fails, however, in describing the electronic properties of many transition metal oxides with half-filled d bands [3]. Mott recognized the importance of electronic correlations in determining the properties of these systems. Intrasite electronic Coulomb repulsion (U) can indeed inhibit delocalization of conduction electrons in systems where the bandwidth (t) is rather small ($t \approx U$). In a system with half-filled bands, correlation results in the splitting of the conduction band into so-called lower and upper Hubbard bands, and the material is turned into a *Mott insulator*.

Materials at half-filling can become insulating also in the presence of electron–phonon coupling through the Peierls

mechanism [4]. In this case a gain in energy is achieved through the dimerization of the lattice, which folds the Brillouin zone, and opens a gap in the conduction band. Many systems (which include several vanadium oxide compounds) experience a lattice distortion in correspondence with the MIT: in this case it becomes unclear whether the principal responsible for the MIT is the Peierls or the Mott mechanism.

The understanding of the electronic properties of strongly correlated electron systems [5] is therefore a long-standing problem. Besides showing insulator to metal transitions, materials with strong electronic correlation also display unusual and remarkable properties, especially in the proximity of the MIT. The discovery of high temperature superconductivity (HTS) in 1986, and of colossal magneto-resistance (CMR) in 1993, boosted the interest in the topic. Since then we have witnessed an impressive advancement in experimental techniques. Out of many, we mention here the development of angle-resolved photoemission [6] and ultrafast (fs) time-resolved spectroscopies [7]. The high brightness of third-generation synchrotron sources enabled the study of systems under extreme experimental conditions such as high pressures, and the development of microscopy at frequencies ranging from x-rays to infrared. Sub-diffraction-limit microscopic techniques have been developed as well. The introduction of a new powerful many-body theoretical tool, such as the dynamical mean-field theory [8], also provided a fundamental contribution in achieving a much deeper understanding of strongly correlated electrons. Thanks to all these progresses, the scientific community today has the opportunity to shed new light on the MIT in the same transition metal oxides which attracted the interest of Mott and Peierls many decades ago.

We address here the electrodynamic properties across the MIT in three different vanadium oxide compounds: V_2O_3, VO_2 and V_3O_5. We induce the MIT either by varying temperature (T) or by applying pressure (P). While being a rather challenging technique, pressure permits us to continuously tune t, thus driving a bandwidth-controlled MIT without introducing impurities or disorder.

The present review is organized as follows. We will first introduce the vanadium oxide systems belonging to the Magnéli phase. After a brief survey of the theoretical framework of strongly correlated electron systems, we will outline the main methodologies used in this work, as for what concerns both experimental techniques and data analysis. The following three sections will be dedicated to the discussion of the optical properties of V_2O_3, VO_2 and V_3O_5, respectively. Finally we will draw some general conclusions and outline future lines of research in the field.

2. Vanadium oxides: the Magnéli phase

The present review is focused on the electrodynamics of the insulator to metal transition in three compounds of the so-called Magnéli phase V_nO_{2n-1} [9]. In particular, we are dealing here with the two end members V_2O_3 ($n = 2$) and VO_2 ($n = \infty$), and an intermediate V_3O_5 ($n = 3$) compound.

VO_2 shows a metallic phase at temperatures larger than the MIT ($T_{MIT} = 340$ K), in correspondence to a rutile-like structure [10]. It is formed by a tetragonal lattice of vanadium ions, each surrounded by a oxygen octahedron. The octahedra are arranged in alternating edge-sharing and corner-sharing chains along the c axis. An equal amount of empty octahedra also forms chains along c. Below T_{MIT} the structure is instead monoclinic and V–V dimers are formed along the c axis.

For $T > 160$ K, V_2O_3 is a metal with corundum structure. Vanadium ions are arranged in a trigonal lattice, and are surrounded by the oxygen octahedra, with no chain formation. The intermediate Magnéli phase compounds, such as, for instance, V_3O_5, can be regarded as rutile-like slabs, separated by planes with a corundum arrangement. These structures can be seen as three-dimensional networks of oxygen octahedra, which are partially filled by vanadium ions.

Because of the slightly different filling conditions and structural arrangements, these compounds display a wide variety of MIT temperatures and magnetic phases (see figure 1). All compounds of the Magnéli phase, with the exception of V_7O_{13}, display a first-order MIT, accompanied by a structural distortion. Interestingly, a magnetic susceptibility anomaly, usually interpreted as a paramagnetic to antiferromagnetic transition, is observed in many compounds of the series. The temperature at which the magnetic anomaly takes place ranges from 160 K ($\simeq T_{MIT}$) in V_2O_3, 75 K in V_3O_5, to zero in VO_2, decreasing almost monotonically along the series.

3. Theoretical framework

The Hubbard model [11], first introduced in 1963, is the prototype model for the description of strongly correlated electron systems. The Hubbard model, in its simplest form, considers a tight-binding Hamiltonian to which is added a repulsive term between electrons occupying the same lattice site i:

$$H = -t \sum_{\langle ij \rangle \sigma} (c_{i\sigma}^+ c_{j\sigma} + h.c.) + U \sum_i n_{i\uparrow} n_{i\downarrow}, \qquad (1)$$

where c^+, c, $n = c^+c$ denote the usual creation, annihilation and number operators, and σ is the spin state. The hopping integral term t is supposed isotropic and non-zero only for nearest-neighbour hopping:

$$t_{ij} = \int \phi_{i\sigma}^*(r) \frac{\hbar^2 \nabla^2}{2m} \phi_{j\sigma}(r) \, dr, \qquad (2)$$

with m being the electron mass and ϕ_{ij} the Wannier orbitals, while the repulsive Coulomb interaction U is defined as

$$U = \int \phi_{i\sigma}^*(r) \phi_{i\sigma}(r) \frac{e^2}{|r - r'|} \phi_{i,-\sigma}(r') \phi_{i,-\sigma}^*(r') \, dr \, dr'. \quad (3)$$

The Hubbard model does not take into account multiband effects. When applied to d orbitals it is implicitly assumed that the orbital degeneracy is lifted out, and the low-energy excitations are described in terms of one single band lying at the Fermi level. When applied to transition metal oxides,
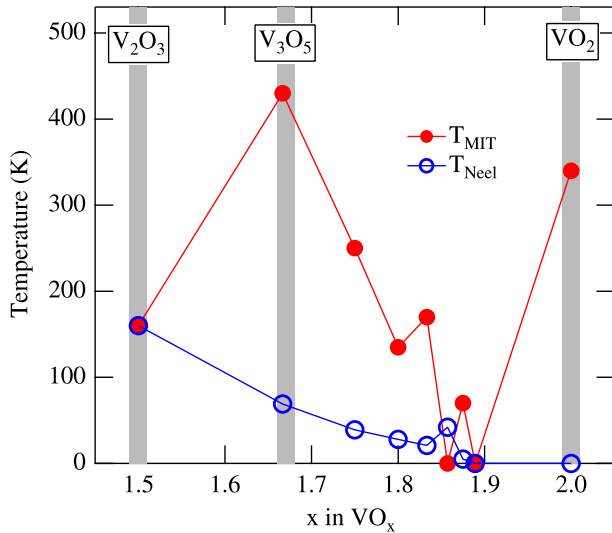
Figure 1. Metal to insulator transition temperatures and magnetic ordering temperatures of compounds belonging to the Magnéli phases [10]. Points related to the compounds under study in the present work have been highlighted.

Figure 2. Sketch of the evolution of the density of states at $T = 0$, with increasing U/t. The first two states correspond to an increasingly correlated metal, while the third one is an insulator [8].

the Hubbard Hamiltonian cannot take properly into account the role of the ligand p band, which has therefore to be considered either far in energy from the relevant metal d band, or completely hybridized with it. Furthermore one has to assume that screening effects completely wash out the interactions extending beyond nearest neighbours.

The Hubbard model is completely solvable in one dimension ($d = 1$), while for $d > 1$ only the limits $U/t \to 0$ and $U/t \to \infty$ can be analytically discussed [12]. In the limit of strong correlation ($U/t \to \infty$), the Hubbard model is equivalent to the Heisenberg model, with $J = \frac{4t^2}{U}$, where in the absence of magnetic frustration an antiferromagnetic state is obtained.

At intermediate values of U/t, the band of the non-interacting system splits into two: the lower and upper Hubbard bands (LHB and UHB), separated by the correlation energy U. The so-called Hubbard approximation reproduces the presence of an MIT at a critical value U_c, when the LHB and UHB merge together, but fails in reproducing the discontinuous character of the MIT, and does not provide a description of the metallic state consistent with the Fermi-liquid properties.

On the other hand, the Brinkman and Rice approach starts from the metallic state, described as a strongly renormalized Fermi liquid, but does not account for the high-energy incoherent excitations responsible for the Hubbard bands, and which should already be present also in the metallic state.

The dynamical mean-field theory (DMFT) is based on the mapping of the full many-body problem onto a quantum impurity model. DMFT takes into account dynamic quantum fluctuations through an energy-dependent Weiss effective field, at variance with the constant one of classical mean-field theory approximations. DMFT permits us to address on an equal footing both the Hubbard bands and quasiparticle bands.

DMFT allows us to progressively follow the progressive separation of the central quasiparticle (QP) peak in the LHB
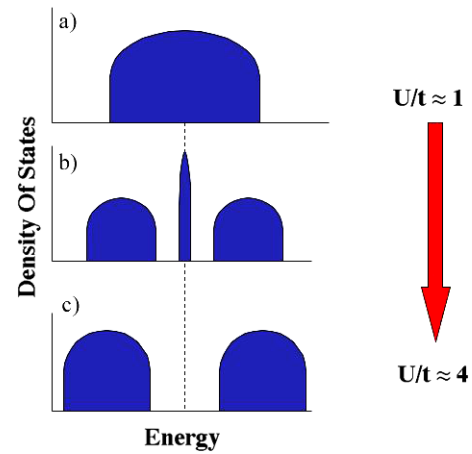
and UHB, as long as U/t is increased. The resulting scenario is schematically sketched in figure 2 for the case $T = 0$. By progressively increasing U/t the Hubbard bands first separate one from the other, while a QP peak still survives at the Fermi energy (figure 2(b)). When U is further increased the peak narrows until it disappears (figure 2(c)) and we are left with the two Hubbard bands only. The vanishing of the QP peak is associated with diverging quasiparticle mass m^*.

It is widely recognized [13] that, in order to correctly describe real materials displaying system-specific localization–delocalization crossover, one needs to incorporate into the DMFT method realistic electronic structure calculations. To this aim, details of the band structure can be used as an input to DMFT, through the so-called LDA + DMFT method [14]. The comparison of the DMFT results with experimental probes of the low-energy electrodynamics, such as photoemission and optical results, is of paramount importance in order to assess the validity of the theoretical approach.

4. Methods

4.1. Optical reflectivity

Optical reflectivity is a very suitable technique to address the physics of strongly correlated electron systems. Optical measurements are contact-free and probe the bulk properties of the system under investigation. This represents an important advantage over more surface-sensitive techniques, especially in the case of strongly correlated electron systems, since it has been proven that local pressure conditions may change the properties of the surface with respect to the bulk [15]. Very recently, it has been shown as well that the presence of dead surface layers are facilitated by strong correlations [16].

Optical reflectivity measurements are normally performed at nearly normal incidence, over a rather broad frequency range, extending from terahertz to the ultraviolet (10–30 000 cm^{-1}). The reference measurement is usually taken on a metallic film (gold or silver, depending on the spectral range) evaporated *in situ* over the sample surface. The

measured reflectivity is then extrapolated towards high and low frequencies by using standard procedures extensively described in [17] and [18]. This allows us to perform a Kramers–Kronig transformation (KKT), from which one can extract the real and the imaginary value of the frequency-dependent conductivity $\tilde{\sigma}(\omega) = \sigma_1(\omega) + i\sigma_2(\omega)$.

At low frequencies, the optical conductivity is normally dominated by the contribution from free electrons, if any. In normal metals this contribution is called the Drude term, and is described by the relation:

$$\tilde{\sigma}_{\mathrm{Drude}} = \frac{1}{4\pi} \frac{\omega_{\mathrm{P}}^2 \tau_{\mathrm{D}}}{1 - i\omega\tau_{\mathrm{D}}}, \tag{4}$$

where $\omega_{\mathrm{P}} = 4\pi N e^2/m$ is the plasma frequency (N being the number of free electrons, e the electron charge and m their band mass) and τ_{D} is the electron scattering time.

Besides the Drude term—normally associated with the coherent motion of charge carriers—other relevant electronic excitations are usually described phenomenologically in terms of Lorentzian harmonic oscillators which take into account electronic interband transitions, through the formula

$$\tilde{\sigma}_{\mathrm{interband}} = \frac{1}{4\pi} \sum_j \frac{\omega_j^2 \omega}{i(\omega_{0j}^2 - \omega^2) + \omega_j \tau_j}. \tag{5}$$

The contribution from the infrared-active phonon modes to the optical conductivity is described as well through Lorentz harmonic oscillators, in the form

$$\tilde{\sigma}_{\mathrm{phonons}} = \frac{1}{4\pi} \sum_l \frac{\omega_l^2 \omega}{i(\omega_{0l}^2 - \omega^2) + \omega_l \tau_l}. \tag{6}$$

The measured optical conductivity is therefore expected to be described as the sum of the three terms $\tilde{\sigma} = \tilde{\sigma}_{\mathrm{Drude}} + \tilde{\sigma}_{\mathrm{interband}} + \tilde{\sigma}_{\mathrm{phonons}}$. While this simple model nicely ties up the physics of most conventional materials, its application to strongly correlated electron systems is much more problematic.

Strongly correlated electron systems in their (bad) metallic phase are indeed characterized by the presence of a broad conductivity term spanning from zero frequency to the mid-and near-infrared range. In order to describe this term, some authors use the so-called *extended Drude model* approach, which makes use of a frequency-dependent scattering rate [19, 20]. Alternatively, one can make use of a two-component description, where the low frequency term is modelled in terms of one Drude plus one harmonic oscillator. In a simple picture, one can figure out these two terms as being associated with the *coherent* motion of quasiparticles and with the *incoherent* transitions from the lower lying electronic bands (Hubbard bands and charge transfer excitations) to the quasiparticle peak and from the quasiparticle peak to higher-energy (Hubbard) bands.

A second characteristic fingerprint of electron correlation is provided by the (apparent) violation of the so-called *f-sum rule*. Indeed, it can be shown that, for any kind of excitation in which charge is involved, the relation

$$\int_0^\infty \sigma_1(\omega)\, d\omega = \frac{\pi}{2} \sum_j \frac{(q_j)^2}{M_j}, \tag{7}$$

holds in which q_j and M_j do represent the electron's charge and mass. The integral in equation (7) should remain constant for any variation of the external parameters (e.g. temperature, pressures, magnetic fields, etc). For obvious reasons, in the real case one has to deal with *partial* sum rules, extending up to the maximum frequency of the measurement. In conventional metals, the *partial* sum rule is well satisfied within frequencies extending up to the plasma frequency [21]. On the other hand, a typical hallmark of strong correlation is the redistribution of the spectral weight within frequencies of several eV. This is seen in optical spectra through a violation of the *partial* sum rule [21, 22], while ellipsometric techniques are normally used to precisely assess the frequency at which the spectral weight is effectively recovered [23].

4.2. Diamond anvil cell

Hydrostatic pressure conditions on the GPa scale are achieved by making use of diamond anvil cells (DACs). DACs consist of two opposing diamonds, with a sample compressed between the diamond's culets. Since pressure scales with the inverse of the area, if one wants to achieve high pressures, the culet area has to be small, i.e. with a diameter of hundreds of microns and below. The combination of the absorption from the diamonds (which have to be type IIa, i.e. nitrogen-free), and the small dimensions of the samples which can be placed in a DAC, make the optical throughput of the whole system rather low. Infrared measurements at high pressure are therefore a very challenging technique, which takes great advantage of making use of an infrared microscope coupled with a high brightness source, such as a synchrotron infrared source [24, 25].

Between the two diamonds of the DAC one places a metallic gasket, which is typically made up of stainless steel (see figures 3 and 4). A hole at the centre of the gasket is filled with a hydrostatic salt transparent to infrared (KBr, NaCl, CsI, etc), together with the sample, and a ruby chip. The latter is used to monitor pressure thanks to its pressure-dependent fluorescent lines. In the case of reflectivity measurements, great care has to be taken in order to prepare a clean and flat sample–diamond interface.

As a reference, one can measure the reflectance from a gold slab mounted inside the cell. Since the intensity reflected by the sample I_{S} and that reflected by the reference I_{Au} are not measured at the same time, in the case of a synchrotron measurement one must take into account the variation of the spectral intensity induced by the decreasing electron beam current. Therefore one can also measure, as an internal correction, the intensity reflected at each pressure by the upper diamond face I_{D}. At the end of the entire pressure run, the gold reference is measured in the DAC with the same procedure, i.e. measuring I_{Au} and I_{D}, respectively. The reflectivity at each pressure is finally obtained by

$$R_{\mathrm{s-d}}(\omega) = \frac{I_{\mathrm{S}}(\omega)}{I_{\mathrm{D}}(\omega)} \frac{I'_{\mathrm{D}}(\omega)}{I_{\mathrm{Au}}(\omega)}. \tag{8}$$

The complex refractive index of the sample $\tilde{n}(\omega)$ is related to the reflectivity measured inside the DAC through the Fresnel formula:

$$R_{\mathrm{s-d}}(\omega) = \left| \frac{\tilde{n}(\omega) - n_{\mathrm{d}}}{\tilde{n}(\omega) + n_{\mathrm{d}}} \right|^2, \tag{9}$$

in which $n_d = 2.43$ indicates the refractive index of diamond [26], assumed to be real and frequency-independent over the whole spectral range considered. However, following equation (9), the pressure-dependent optical properties are not unequivocally determined from R_{s-d}. In order to fully characterize optical properties of the sample and calculate the optical conductivity one can either fit $R_{s-d}(\omega)$ within the Drude–Lorentz framework, measure simultaneously reflectance and transmittance, or perform Kramers–Kronig transformations.

4.2.1. Lorentz–Drude fitting. Formula (9) can be easily written in terms of the complex dielectric constant or refractive index, following basic relations between optical constants [17]. If one models the optical conductivity within the Lorentz–Drude framework as described in the previous paragraph it is then possible to directly fit the R_{s-d} data and to recalculate all the optical constants of interest.

However, a direct fit on the reflectivity is not straightforward, since—at variance with $\tilde{\sigma}(\omega)$—reflectivity is not an additive quantity. An *a priori* knowledge of $\tilde{\sigma}(\omega)$, at least at zero applied pressure, is therefore a desirable requirement in order to identify the relevant harmonic oscillators of the case.

4.2.2. Kramers–Kronig transformations. The application of KKT to reflectivity measurements performed in a DAC is not straightforward as well. This is first due to the fact that, in most cases, the measured spectral range is more limited with respect to conventional ambient pressure data. Second, standard KKT need to be corrected by using an *a priori* unknown parameter (ω_β) in order to take into account the presence of the sample–diamond interface [27–29].

In order to overcome the first problem a Lorentz–Drude fitting is normally performed *before* running KKT. The fit helps to establish the expected shape of R_{s-d} in the spectral regions where data are missing. Once the proper R_{s-d} shape has been recovered over a sufficiently broad range one can then apply the relation

$$\phi(\omega_0) = -\frac{\omega_0}{\pi} P \int_0^{+\infty} \frac{\ln R_{s-d}(\omega)}{\omega^2 - \omega_0^2} d\omega + \left[\pi - 2 \arctan \frac{\omega_\beta}{\omega_0} \right], \quad (10)$$

where ω_β is the position of the reflectivity pole on the imaginary axis in the complex frequency plane. The ω_β term is present in standard sample–vacuum (i.e. ambient pressure) KKT as well, but tends to infinity, which makes the right-hand side of equation (10) vanish. In the case of reflectivity measurements in a DAC, the criterion used to properly evaluate ω_β is the agreement between the KKT result and the initial fit [27–29].

The above-mentioned procedure is certainly not free of uncertainties, since it strongly relies on the fitting results. However, its use permits us to get rid of artefacts which may result from artificial constraints imposed by the Lorentz–Drude phenomenological model. The KKT in a DAC have been successfully used in [27, 28] and [29] in order to reliably discuss power laws in the pressure-dependent $\sigma_1(\omega)$.
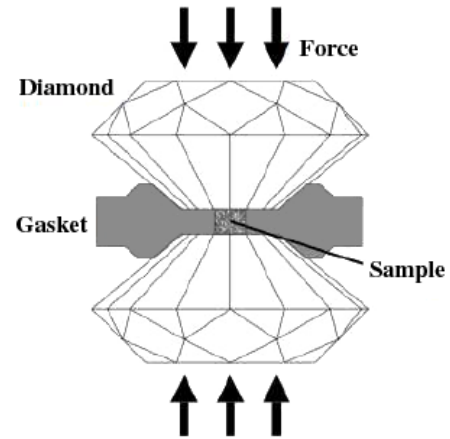

Figure 3. Schematic representation of a diamond anvil cell.

4.2.3. Measurement of reflectance and transmittance. In some cases, the sample filled in the DAC may be so thin that light is partially transmitted through it. In this case one should take great care in adopting the techniques discussed above (normally well suited to semi-infinite media), and take into account the effects from the finite thickness of the sample. If, together with R_{s-d}, one is able to measure at each pressure the transmittance of the sample, it is possible to fully determine analytically the optical properties of the system. To this aim, a multilayer scheme of diamond–sample–salt–diamond can be adopted, where the multiple reflections within the sample and the salt layer can be accounted for by adding incoherently the intensities of the reflected beam. The analytical derivation under the above assumptions is straightforward, albeit rather lengthy, and has been successfully applied in the present study to determine the properties of vanadium dioxide samples.

5. Vanadium sesquioxide—V$_2$O$_3$

5.1. Properties and phase diagram

Many authors consider vanadium sesquioxide as *the* prototype of strongly correlated compounds. Its temperature versus alloying phase diagram (reported in figure 5) displays the presence of three main phases: antiferromagnetic insulator (AFI), paramagnetic insulator (PI) and paramagnetic metal (PM). The PI phase is accessed via Cr alloying of V$_2$O$_3$ at temperatures higher than the Néel temperature. A critical point is also present in the phase diagram, above which one enters the so-called *crossover* phase. Note that alloying V$_2$O$_3$ with Ti (Cr) is considered equivalent to the application of positive (negative) pressure to the pristine vanadium sesquioxide [31–35].

V$_2$O$_3$ crystallizes in the corundum structure, with the V ions surrounded by O octahedra. The V ions form a honeycomb lattice within the *ab* plane, while tending to form dimerized chains along *c*. Their oxidation state is V^{3+}, with 3d^2 configuration. The crystal field splitting to the O octahedra separates two upper e$_g^\sigma$ and three lower t$_{2g}$ orbitals. Trigonal distortions induce a further split of the t$_{2g}$ orbitals in the upper a$_{1g}$ and the two lower degenerate e$_g^\pi$. The former
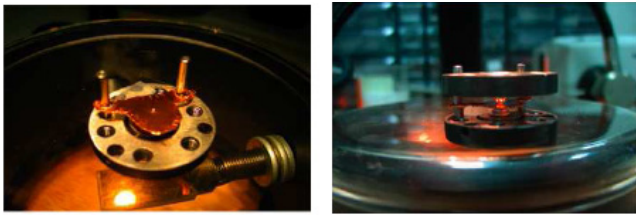
Figure 4. Pictures of the open (left panel) and closed (right panel) DAC with a copper gasket.
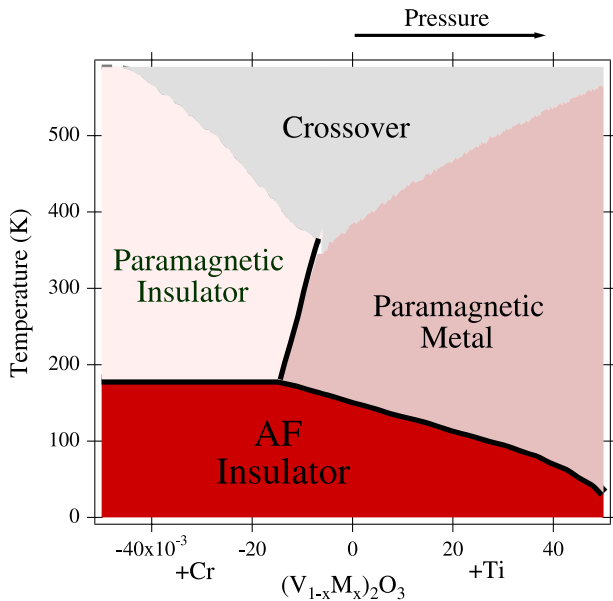

Figure 5. Phase diagram of V_2O_3 showing the MIT as a function of alloying with Cr and Ti. After [30].

Figure 6. (a) Near-normal incidence reflectivity of V_2O_3 shown at selected T between 0 and 20 000 cm^{-1}. (b) Optical conductivity obtained from the reflectivity in (a), plotted in the same spectral range, for the same T. Reprinted with permission from [38]. Copyright 2008 by the American Physical Society.

orbital is mainly directed along the c axis and therefore is supposed to mediate the strong hybridization between the V–V dimers. Such strong hybridization led to a model, established by Castellani *et al* [41], where two of the four electrons per V–V pair occupy a bonding molecular orbital formed by a_{1g} states. Since the two remaining electrons place themselves in a partially filled twofold-degenerate e_g^π state, V_2O_3 has long been treated as a system with a half-filled single band. This modelling, which leads to a spin-1/2 orbital degenerate state with a complex orbital and spin ordering [41], has been challenged [42] by means of linear dichroism that revealed a high spin state. Moreover it was shown that the V ion ground state is predominantly $e_g^\pi e_g^\pi$ with a small admixture of $e_g^\pi a_{1g}$ [42]. It is now accepted that to describe the physical properties of V_2O_3 it is necessary to go beyond the half-filled single-band picture, as will be discussed in the following.

5.2. V_2O_3 versus temperature

We discuss in this section the optical properties of V_2O_3 as a function of temperature. The seminal work from Rozenberg *et al* [36] attempted a description of the optical properties of V_2O_3 by taking into account correlation effects while ignoring the degeneracies of the bands. Many important features of the
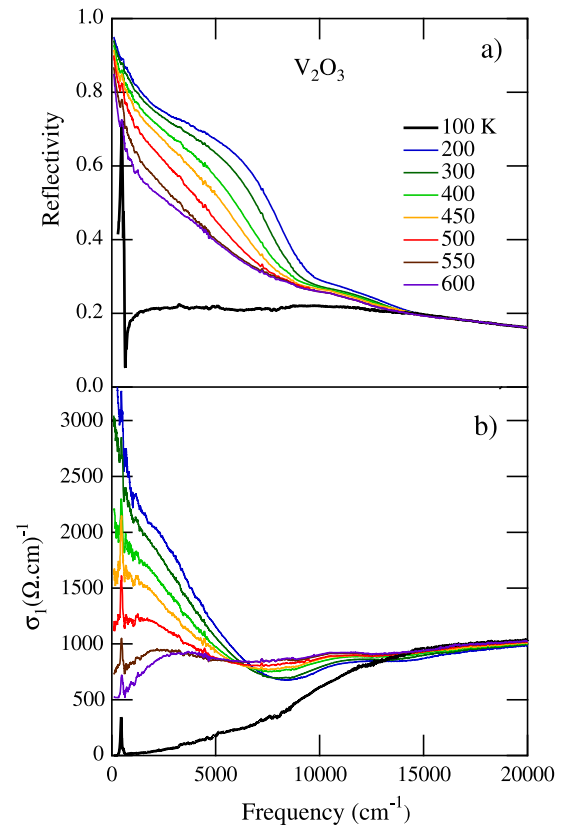
physics of V_2O_3 were indeed successfully resolved by their model for the first time. However, it is widely recognized that, in order to fully understand the properties of V_2O_3, multiband effects have to be carefully taken into account [40, 37]. A substantial extension of the data from [36] (which were limited to three temperatures only) is reported in [38]. Therein, the optical properties of high quality single crystals of V_2O_3 are shown and discussed in the AFI, PM and up to the *crossover* phase.

The results are reported in figure 6(a) at selected temperatures. Below T_N, with the exception of a phonon peak at about 500 cm^{-1}, $R(\omega)$ is nearly flat up to 10 000 cm^{-1}, where a weak electronic absorption band appears. On the other hand, while entering into the PM phase ($T \geqslant 200$ K), the reflectivity is much more enhanced, with $R(\omega) \rightarrow 1$, as a signature for metallization. With further increasing temperature, $R(\omega)$ decreases over the whole frequency range, while maintaining a substantially metallic (though overdamped) behaviour. Above 15 000 cm^{-1} the reflectivity curves at all temperatures merge together.

Let us now turn to the optical conductivity curves in figure 6(b), obtained through KKT. $\sigma_1(\omega)$ at 100 K, i.e. in the AFI phase, shows a well-defined charge gap of about 1 eV, which is in very good agreement with data from [36] and is ascribed to excitations from the lower to the upper Hubbard band. Above T_N, the gap is abruptly filled by the

appearance of a large term extending from dc to approximately 1 eV. As we have discussed previously, this term seems to be made up of two major components: one sharp Drude-like feature associated with the *coherent* QP's motion, and one large *incoherent* mid-infrared band. On further increasing temperature $\sigma_1(\omega)$ presents a strong temperature dependence, displaying a transfer of spectral weight from low to high frequencies through an isosbestic point at about 6000 cm^{-1}. Besides the spectral weight transfer, a very notable feature is the continuous depletion of $\sigma_1(\omega)$, as temperature increases. Not only $\sigma_1(\omega)$ decreases, but it also changes curvature, with a clear sign change of the derivative $(d\sigma_1(\omega)/d\omega \geqslant 0)$ above 450 K. At 600 K, the downturn transforms into a pseudogap at low frequency, while the mid-infrared band broadens. The pseudogap formation nicely agrees with the anomalous enhancement of the resistivity, while entering into the *crossover* regime. Such behaviour can be understood as being related to the disappearance of the QPs because of their loss of coherence above $T_{\mathrm{coh}} \simeq 425$ K.

The optical spectral weight (SW) has been calculated through the restricted f sum rule [17]:

$$\mathrm{SW}(\Omega, T) = \frac{2mV_V}{\pi e^2} \int_0^\Omega \sigma_1(\omega, T) \, d\omega, \tag{11}$$

where m is the mass of the carriers, e is the electron charge and V_V is the volume per V ion. We report in figure 7(a) the temperature behaviour of SW, normalized at 200 K for three different Ω cutoff values. In the AFI state the SW is nearly zero and shows a large discontinuity at T_N, due to the appearance of QPs. On further increasing T, SW decreases, mainly reflecting the loss of coherence of the QP contribution.

Between 200 and 550 K, the SW scales as T^2 (see figure 7(b)), following the relationship [21, 22]

$$\mathrm{SW}(\Omega, T) = \mathrm{SW}(\Omega, 0) - B(\Omega)T^2, \tag{12}$$

where $B(\Omega)$ depends on the effective QP bandwidth, thus providing an estimate of the strength of the correlations. Such a behaviour, characteristic of a Fermi liquid, has been observed in cuprates as well. By defining $b(\Omega) = B(\Omega)/(\Omega, 0)$, we obtain $b(8000 \text{ cm}^{-1}) = 1.6 \times 10^{-6}$ K^{-2}. This value is larger than that found in the La$_{2-x}$Sr$_x$CuO$_4$ cuprate [21] ($b = 2.5 \times 10^{-7}$ K^{-2}), and comparable to other strongly correlated compounds [39] such as Nd$_{0.905}$TiO$_3$ ($b = 2.2 \times 10^{-6}$ K^{-2}). We note for reference that a conventional metal like gold [21] takes a much lower b value ($b = 1.3 \times 10^{-8}$ K^{-2}).

One may ask how well the single-band half-filled Hubbard model is able to reproduce the observed results at high temperatures. By using the same effective U values as in [36] ($U = 2D$ for the PM and $U = 4D$ for the AFI phase, D being the half-bandwidth), it is found that the Hubbard model provides correct estimates for the high temperature decrease, i.e. 40%–70% for the different cutoffs (see figure 7(c)). However, the T scale is off by a factor of 2, thus confirming the need for a more complicated theoretical description.

The chance to go beyond a single-band theoretical discussion is provided by combining LDA + DMFT [40]. Tomczack and Biermann [44, 38] discussed the optical
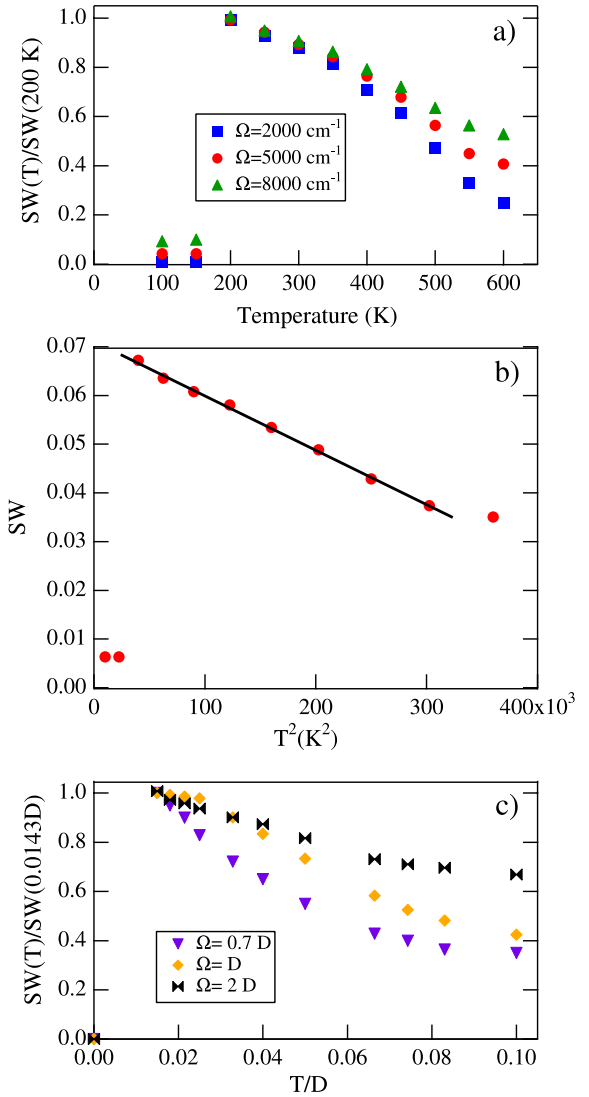

Figure 7. (a) Experimental SW(T, Ω) for three different cutoffs Ω as a function of T. (b) SW(T, Ω) for $\Omega = 8000$ cm^{-1} as a function of T^2, showing a linear behaviour. (c) SW(T, Ω) from the single-band Hubbard model. The normalization of the theoretical data coincides with the experimental one if $D = 1$ eV. Reprinted with permission from [38]. Copyright 2008 by the American Physical Society.

properties of V$_2$O$_3$ by taking into account independently the role of the e$_g^\pi$ and a$_{1g}$ within DMFT. Following the theoretical framework described in [45], the authors assert that the e$_g^\pi$ excitations are not coherent down to 390 K, while a$_{1g}$ carriers are. By raising the temperature one therefore expects a larger impact on the a$_{1g}$-derived carriers and their consequent loss of coherence. Indeed, the optical response below 0.6 eV, which is dominated by the a$_{1g}$–e$_g^\pi$ transitions, will be more temperature-dependent than that above 0.6 eV, which is mainly due to e$_g^\pi$–e$_g^\pi$ transitions. Following [44], this can explain, at least qualitatively, the opening of the pseudogap in the optical conductivity. Note that, while the multiband model depicts a different scenario with respect to the single-band picture, the mid-infrared band observed in the optical spectra is explained in both cases as being due to transitions between a coherent peak at the Fermi level and an incoherent band (i.e. from the a$_{1g}$ to the lower lying e$_g^\pi$, in the multiband case).
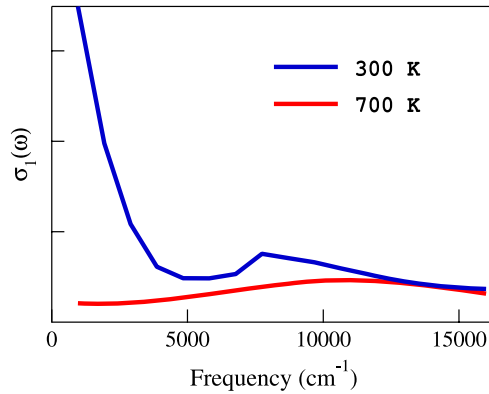
Figure 8. Optical conductivity for V_2O_3 at three different temperatures with LDA + DMFT, calculated by taking into account the experimental values of the lattice parameters [30]. Reprinted with permission from [38]. Copyright 2008 by the American Physical Society.

A further improvement in the theoretical description of V_2O_3 has been made by taking into account the experimentally observed change of the lattice parameters as a function of temperature [30]. In particular, the c/a ratio is of the order of 2.835 at room temperature, but decreases below 2.800 at temperatures higher than 600 K. Considering this experimental fact, the LDA + DMFT calculation at 300 and 700 K can be fed with the *real* data for the lattice parameters. As a result of the distortion the LDA bandwidth shrinks and the optical conductivity from DMFT (see figure 8) displays the presence of a well-defined pseudogap, in agreement with the experimental data shown in figure 6(b). It is important to observe that, if the lattice parameter values at 300 K were used in the high temperature DMFT calculation, the optical conductivity at 700 K would have displayed a strongly renormalized Drude-like peak, instead of the pseudogap.

Ellipsometric measurements on 75 nm thick V_2O_3 films grown on $(10\bar{1}0)$-oriented sapphire substrates have also been carried out recently by Qazilbash *et al* [23]. In this work measurements are performed up to 6 eV between 100 and 400 K. The shape and trends of the optical conductivities are very much similar to the data of figure 6(b), while their absolute values are sizeably lower. In particular, the Drude QP peak (labelled v in [23]) is barely distinguishable from the incoherent band (w) in the ellipsometric measurement. This difference is likely attributed to the larger resistivity of films with respect to single crystals in the metallic state [46]. The ellipsometric study permits to thoroughly assign all the interband transitions within the many-fold V 3d bands. The highest-energy feature, at about 4.5 eV, is ascribed to charge transfer excitations. The spectral weight variation between PM and AFI phases is still not completely recovered at 6 eV, thus underlying the very large correlation effects in V_2O_3.

6. Vanadium dioxide—VO_2

6.1. Properties

Vanadium dioxide has attracted the greatest attention for many decades [47]. The presence of an MIT transition involving a resistivity jump of two orders of magnitude, close to room temperature (340 K, 67 °C), makes it extremely appealing from a technological point of view. Vanadium dioxide is indeed already in use in the fabrication of thermochromic windows, and is a very promising material to be used as a micro-thermometer or for the realization of ultrafast electro-optical switches.

Since the electronic transition is accompanied by a structural one, from monoclinic to rutile, it has long been debated whether the transition is due to the Mott–Hubbard or to the Peierls mechanism: the monoclinic (M1) phase displays indeed, along the c axis, a tilted V ion dimerization. The metal to insulator transition of VO_2 has been intensively investigated also in recent years thanks to new advances in several instrumentation techniques. Out of many we mention femtosecond time-resolved studies, both at optical [48] and THz frequencies [49, 50], optical spectroscopy at high pressures [51, 52] and scanning near-field infrared microscopy (SNIM) [20]. These recent research studies seem to indicate that the major role in the MIT of VO_2 is played by the Mott–Hubbard mechanism.

Vanadium dioxide is in the $3d^1$ electronic configuration. Similarly to V_2O_3, the total crystal fields split the d orbitals into two e_g^σ, two e_g^π and one a_{1g}. In the rutile phase all these orbitals overlap, while in the M1 phase the a_{1g} orbital is further split into two because of the dimerization. However, LDA calculations miss the real physics of VO_2, since a metallic ground state is predicted for both structures [53].

Several temperature-dependent optical studies have been performed on VO_2 [55, 56, 54, 23, 57, 58] on both single crystals and thin films. In their seminal work Verleur *et al* [56] identified the presence of four prominent absorption peaks (at energies of about 0.85, 1.3, 2.8 and 3.6 eV) in the insulating phase, as well as a metallic-like feature and two absorption peaks (near 3 and 4 eV) in the metallic phase. In the same paper a comparison of the optical properties of single crystals and thin films is also performed, showing that there is an overall agreement in the structural features, though some differences in the magnitude of the optical constants is found [56]. The results of Qazilbash *et al* [54] are in agreement with previous literature [56–58] and extend the study of the optical properties of VO_2 also at high T. The authors investigate the properties of the free carriers beyond the Ioffe–Regel limit [54] and conclude that electron–electron and electron–phonon coupling may not be treated on the same footing in VO_2, the charge dynamics being dominated by electronic correlation.

A detailed study of the redistribution of SW on a thin film of VO_2 across the MIT may be found in [23]. The development of a Drude-like term, such as $T > T_{MIT}$, coincides with a strong loss of spectral weight at frequencies above 1.3 eV. This transfer of SW is attributed to the changes in the optical conductivity below 4 eV because of the rearrangement of the a_{1g} and e_g^π bands across the transition. The spectral weight of the Drude-like feature is thus obtained from the loss of the SW of the transitions between the filled lower a_{1g} band to the empty e_g^π and to the narrow unoccupied a_{1g} band that characterize the optical properties of the monoclinic insulating phase. Additional SW is transferred to the Drude-like absorption from the optical transitions between the O(2p)
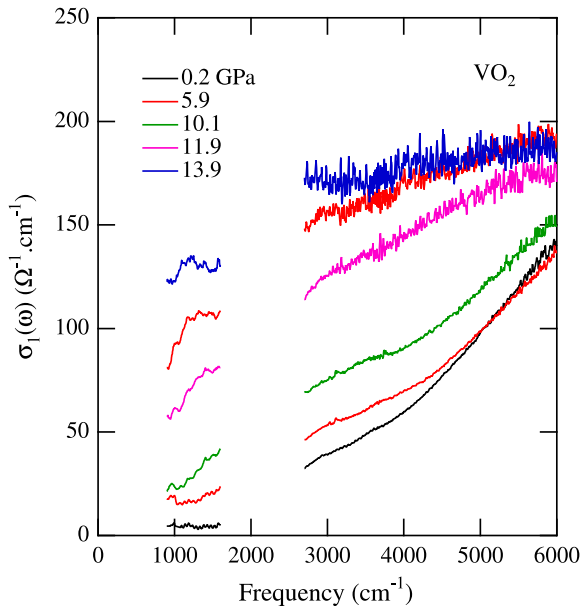
Figure 9. Pressure-dependent optical conductivity of VO$_2$. Reprinted with permission from [51]. Copyright 2007 by the American Physical Society.

bands and vanadium a$_{1g}$ and e$_g^\pi$. Indeed, since the latter are partially filled in the rutile phase, the SW of this optical absorption is partially reduced.

The spectral weight redistribution across the MIT extends to frequencies larger than 6 eV as convincing evidence for the dominant role of electronic correlation in this compound. In a narrow temperature range around the MIT insulating and metallic nanosized islands have been observed to coexist through scanning near-field infrared microscopy (SNIM) [20]. Morphologic information about these islands combined with spatially averaged spectroscopic data provided the temperature dependence of the quasiparticle mass which tends to diverge by approaching the MIT [20]. A rather large mass enhancement is found also by Okazaki and co-workers [57], thus strongly supporting the predominant role of correlation in the electrodynamics of VO$_2$.

Theoretical calculations by Biermann *et al* [53] showed that the physics of VO$_2$ may be captured correctly with a cluster extension of DMFT in combination with density functional theory. This method, accounting explicitly for the V–V dimers, allows to obtain an insulating gap in the monoclinic phase of VO$_2$ for reasonable values of U (∼4 eV). The optical properties of VO$_2$ have also been calculated within an LDA + DMFT by the same authors [59], showing good agreement with the temperature-dependent experimental data [56, 54, 57].

6.2. VO$_2$ versus pressure

In order to shed more light on the subtle interplay between Peierls and Mott–Hubbard mechanisms with respect to the MIT, the optical conductivity of V$_{1-x}$Cr$_x$O$_2$ has been studied, at various Cr contents x, as a function of pressure at room temperature [51]. The preparation of thin V$_{1-x}$Cr$_x$O$_2$ pellets permitted us to measure simultaneously the reflectance and
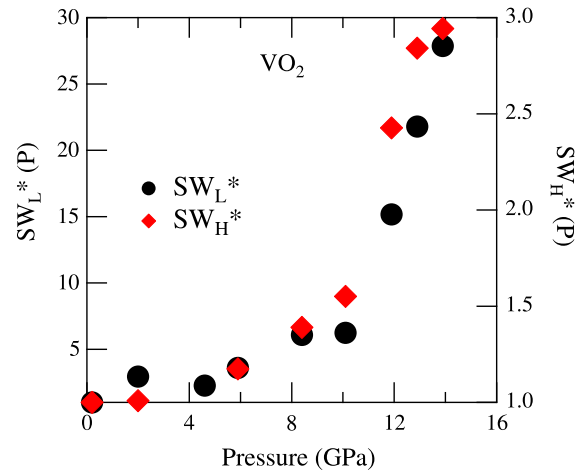

Figure 10. Normalized spectral weights SW$_L$ and SW$_H$, as defined in the text. Reprinted with permission from [51]. Copyright 2007 by the American Physical Society.

transmittance in the infrared (see section 4.2.3) and to calculate $\sigma_1(\omega)$ through a numerical iterative procedure [51, 52].

For the pure VO$_2$ material, at the lowest applied pressure (0.2 GPa), $\sigma_1(\omega)$ presents a main gap feature slightly below 0.5 eV (in good agreement with the ambient pressure measurement [23]), followed by a smooth absorption tail extending down to 1500 cm^{-1} (0.2 eV). The spectra are weakly pressure-dependent up to 4 GPa. On further increasing pressure the optical conductivity slightly increases up to 10 GPa. Above this pressure an abrupt increase of $\sigma_1(\omega)$ is observed, together with a partial filling of the insulating gap, at least at mid-IR frequencies. A rough linear extrapolation of the data collected above 10 GPa gives positive, although small, $\sigma_1(\omega = 0)$ values, compatible with a bad metallic behaviour.

In order to better highlight the pressure dependence of the data, the frequency integral of $\sigma_1(\omega)$ over 900–1600 cm^{-1} [SW$_L$(P)] and 2600–5000 cm^{-1} [SW$_H$(P)] was calculated at each pressure. The integration has not been extended above 5000 cm^{-1}, owing to the onset of saturation effects in the spectra collected at the highest pressures (see the high noise level in figure 9), which makes the extraction of the optical conductivity less reliable. In figure 10 the spectral weights normalized to the lowest pressure values, SW$_L$(P) = SW$_L$(P)/SW$_L$(0) and SW$_H$(P) = SW$_H$(P)/SW$_H$(0), are reported. Both quantities show the same pressure dependence, with an abrupt change of slope at 10 GPa. The enhancement of SW$_L$(P) is much larger than that of SW$_H$(P), as expected for a charge delocalization process. While data at far-infrared frequencies would be desirable in order to provide a better estimate of $\sigma_1(\omega = 0)$, the present results are a strong indication for the occurrence of a pressure-induced MIT above 10 GPa.

The same samples were also studied as a function of pressure by Raman spectroscopy [51]. At ambient pressure, 15 narrow phonon lines of the 18 Raman-active modes predicted for the monoclinic M1 phase are identified. Applied pressure results in a phonon frequency hardening, with no significant change in the overall peak pattern. Since the Raman spectrum of VO$_2$ in the rutile (R) phase is characterized by four broad
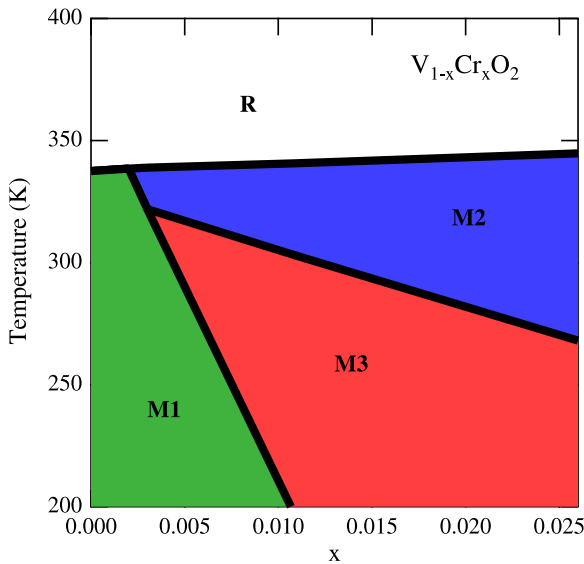
Figure 11. Phase diagram of $V_{1-x}Cr_xO_2$ as a function of temperature and Cr concentration, following [60]. The abbreviations R, M1, M2 and M3 stand for the rutile and monoclinic (1, 2, 3) structural phases, respectively, as described in the text.

Figure 12. Pressure-dependent optical conductivity of 0.025% Cr-doped VO$_2$. Reprinted with permission from [52]. Copyright 2008 by the American Physical Society.

Figure 13. Normalized spectral weights SW$_L$ and SW$_H$ for 0.025% Cr-doped VO$_2$. Reprinted with permission from [52]. Copyright 2008 by the American Physical Society.

peaks only, it is concluded that, by applying pressure up to 19 GPa (i.e. the highest applied pressure value), no transition to the R phase (or to a more symmetric phase than M1) is achieved. A more careful analysis of the Raman data shows that all phonon peaks except ω_{V1} (at 192 cm^{-1}) and ω_{V2} (at 224 cm^{-1}) increase almost linearly with pressure. It is found indeed that both ω_{V1} and ω_{V2} experience a rather abrupt change in dω/dP at 10 GPa. While dω/dP is close to zero at low pressures, it increases to 1–1.5 cm^{-1} GPa^{-1} above 10 GPa. Following the absence of the oxygen isotope effect in the Raman measurement in [52], these two modes are assigned to V ion motion along the c axis. It is therefore tempting to attribute the above-mentioned change of slope as a consequence of a rearrangement of the V dimers as the pressure is increased above 10 GPa.

6.3. Cr–VO$_2$ versus pressure

A further insight into the physics of VO$_2$ can be gained by addressing Cr-substituted compounds. The $V_{1-x}Cr_xO_2$ phase diagram as a function of the Cr substitution fraction x and temperature is displayed in figure 11. As seen in the phase diagram, the T_{MIT} increases only slightly as a function of Cr substitution. Most notable are the transitions observed at room temperature and below, between three distinct monoclinic insulating phases. In the M2 phase only one-half of the V atoms dimerizes along the c-axis direction, while the remaining V ions form zigzag chains of equally spaced atoms. The M3 phase is somehow intermediate between M1 and M2: the dimerized chain starts to tilt and the zigzag chains gets partially dimerized. The M3 phase, often also called the T phase, was explained in terms of two V sublattices within a triclinic structure [61]. The M2 and M3 phases can also be regarded as metastable phases of pure VO$_2$, with a free energy which is only slightly larger than that of M1 [62].
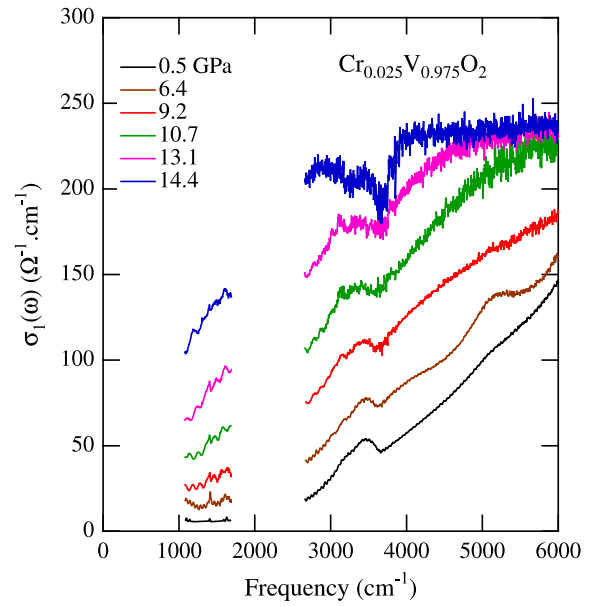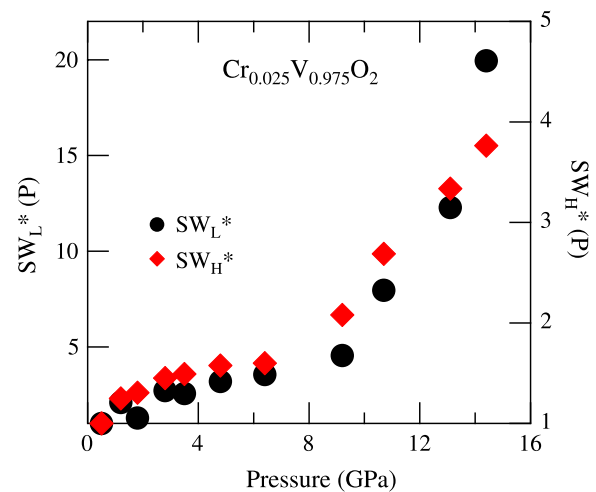
Infrared measurements on a $V_{0.975}Cr_{0.025}O_2$ pellet as a function of pressure were performed with the same technique as described above for pure VO$_2$. Following the phase diagram of figure 11, the substitution of 0.025% Cr stabilizes the M2 phase at ambient conditions. The shape of $\sigma_1(\omega)$ of the Cr-substituted sample displayed in figure 12 is very similar to that of the pristine sample. Again, the conductivity at the lowest pressure is gapped and a strong enhancement of $\sigma_1(\omega)$ is observed above 10 GPa, as an indication of a pressure-induced MIT. The absolute values of the normalized spectral weights (shown in figure 13) are almost the same for both samples, even though, in the case of the Cr-doped sample only, a slight increase is observed also at low pressures.

While infrared measurements show a substantial similarity in the electronic properties of the two compounds, Raman

10

spectra are of great help in order to underline their structural differences. It is found indeed that at ambient pressure conditions the pure and 0.025% Cr-doped compound display distinct phonon peak patterns, as a consequence of their different monoclinic arrangements (i.e. M1 and M2, respectively). The same is true also for the $x = 0.007$ (M3) compound, displaying a Raman pattern intermediate between the two. By applying pressure, the Raman spectra of the three compounds progressively merge. For the $x = 0.007$ compound one observes a continuous transition towards the M1 phase, which is completed at about 3 GPa. Similarly, the $x = 0.025$ sample completes its structural transition at 9 GPa. Such a difference in the transition pressure values reflects the larger structural changes between the phases M2 and M1, with respect to the intermediate phase M3.

An accurate inspection of the pressure dependence of the most relevant phonon modes leads us to conclude that pressure progressively compresses and symmetrizes oxygen octahedra of the three samples, which then get more and more similar between each other. On further increasing pressure above 9 GPa, the pressure dependence of the ω_{V1} and ω_{V2} modes changes slope for all the samples considered. This suggests a slight rearrangement of the V chains, leading to a common metallic monoclinic phase (M_x), where the extent of the Peierls distortion is still unknown. However, the metallic state in the M_x phase is completely different to that observed in the rutile symmetry. In this case a robust Drude term shows up in the infrared conductivity surviving also at the highest measured temperature ($T \simeq 450$ K) [23]. Meanwhile this term in absent in our case.

The combination of high pressure infrared and Raman results outline a scenario where the pressure-induced metallization process occurs within the monoclinic symmetry, which retains well above 15 GPa (at least up to 19 GPa for VO$_2$)[3]. The structural differences observed between the various monoclinic phases have a very small impact on the electronic properties, as observed through infrared. As suggested by the Raman measurement, above 10 GPa the unit cell volume abruptly decreases for all the considered Cr concentrations, which suggests a common lattice instability within the monoclinic symmetry. Since the monoclinic to rutile structural change is considered as the signature for the Peierls transition in VO$_2$, the present results support the major role of electron correlations against structural effects in driving the MIT.

7. V$_3$O$_5$

7.1. Properties

V$_3$O$_5$ is an intermediate member of the Magnéli phase, undergoing a metal to insulator transition [64] for $T_{MIT} = 428$ K. At T_{MIT}, the resistivity sharply drops by more than two orders of magnitude, but dρ/dT remains negative, thus indicating an activated transport behaviour also in the metallic state [65]. The activation energy determined through resistivity

---

3 Preliminary high pressure x-ray diffraction data extend the stability of the monoclinic phase up to 42 GPa [63].

measurements, which is 0.3 eV in the low temperature insulating phase, is reduced to 0.13 eV in the high temperature state.

As in the case of V$_2$O$_3$ and VO$_2$, the phase transition is accompanied by a structural rearrangement of the lattice, leading to the symmetry change $P2/c \rightarrow I2/c$ and to a reduction in the unit cell size of about 0.14% [65, 66]. The monoclinic crystal structure is made up of oxygen octahedra surrounding the vanadium atoms. These octahedra form two types of alternating one-dimensional chains [66, 67]: one chain (A) is composed by double octahedra sharing a face, where these double octahedra are coupled together by sharing edges. The other chain (B) is made up of single corner-sharing octahedra. The chains A and B are mutually connected by sharing both octahedral edges or corners. At high temperature, two different kinds of octahedra (V(1) and V(2)) have been identified, which split into four below T_{MIT} (V(11), V(12), V(21), V(22)) [66, 67]. Following [66], in the insulating phase, the V(11) octahedra host the V^{4+} ions while in the three other kinds of octahedra V^{3+} ions are found. The V(1) octahedra can host either V^{3+} or V^{4+} vanadium ions, with a 3.5 mixed valence, while in V(2) octahedra there are only V^{3+} ions. V(1) octahedra occupy the chains made of double octahedra, while V(2) compose the single octahedra chains. Besides hosting in the low-T phase only V^{4+} ions, V(11) is by far the smallest and more distorted octahedron.

The MIT seems therefore to be driven by charge disproportion and spatial ordering of the V^{4+} and V^{3+} ions [65]. It has been argued [65] that the mechanism involved in the transition may be similar to that of the so-called Verwey transition [68] observed in magnetite (Fe$_3$O$_4$). Scenarios involving the formation of a polaronic Wigner crystal below T_{MIT}, and its melting at high temperatures, have therefore been put forward [65].

A transition from an antiferromagnetic to paramagnetic phase [69] is also observed within the insulating phase at $T_N = 75$ K. Since $T_{MIT} \gg T_N$, the MIT appears to be decoupled from the AF order. Therefore V$_3$O$_5$ is a suitable system to study the charge dynamics near a metal-to-insulator transition without any charge localization induced by magnetic effects.

7.2. V$_3$O$_5$ versus temperature

The temperature-dependent optical reflectivity measured at nearly normal incidence is reported in figure 14(a). For temperatures up to 373 K, $R(\omega)$ is nearly constant for $\omega < 250$ cm^{-1}. Above T_{MIT}, $R(\omega)$ increases continuously, with $R(\omega) \rightarrow 1$, for $\omega \rightarrow 0$, as evidence for metallic behaviour.

The optical conductivity extracted through KKT is shown in figure 14(b). At low temperatures, $\sigma_1(\omega)$ displays a clear insulating behaviour, with a gap-like feature and a mid-IR (MIR) band. No major change is observed in the conductivity while crossing T_N, at variance with that of V$_2$O$_3$ (see section 5.2), thus indicating the low sensitivity of the electronic properties of V$_3$O$_5$ to the magnetic ordering. The MIR band continuously narrows and shifts towards low frequencies while heating from 10 to 300 K. As is better highlighted in figure 15, this trend is much more pronounced between 300 K and T_{MIT}.
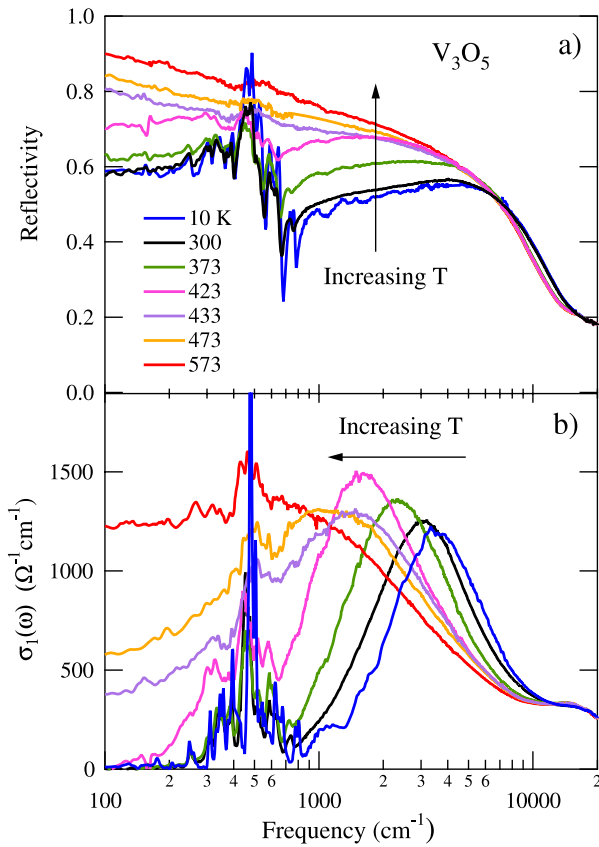
Figure 14. (a) Optical reflectivity of V_3O_5 between 100 and 20 000 cm^{-1} at selected temperatures. (b) Real part of the optical conductivity at the same temperatures and over the same spectral range, as extracted from KKT. Reprinted with permission from [70]. Copyright 2007 by the American Physical Society.

Figure 15. The MIR peak frequency (ω_{MIR}) and its half-width at half-maximum (Γ_{MIR}) as a function of temperature are shown. The values have been obtained by a Drude–Lorenz fit of the optical conductivity (see text). Reprinted with permission from [70]. Copyright 2007 by the American Physical Society.

Figure 16. Optical spectral weight of V_3O_5 as a function of frequency at given temperatures. Reprinted with permission from [70]. Copyright 2007 by the American Physical Society.

The peak value of the MIR band drops from 3000 cm^{-1} at 300 K to 1000 cm^{-1} at the highest temperature (573 K). In the following, these two energy scales are defined as HF-MIR and LF-MIR, respectively. On the other hand, the width of the MIR band (Γ_{MIR}, defined at half-width at half-maximum) abruptly increases above T_{MIT}, possibly indicating that a more disordered state is generated in the high temperature phase.

In the high temperature state, $\sigma_1(\omega = 0) \neq 0$, as a consequence of the MIT. However, the conductivity cannot be described by a Drude term. Indeed a low frequency flat background (causing the non-zero dc conductivity) is superimposed to a mid-IR absorption centred at about 1000 cm^{-1} (LF-MIR), thus suggesting an incoherent transport mechanism to be responsible for the low-energy charge dynamics in this compound.

The spectral weight at the various temperatures is reported in figure 16. The SW is strongly temperature dependent below 5000 cm^{-1}, whereas the *f-sum rule* is fully satisfied above 8000 cm^{-1}. This behaviour is very much similar to that of Fe_3O_4 [71]. In that case the charge-ordered ground state is attributed to polaronic localization and ordering. The energy scale of the SW recovery in these compounds (1 eV) is small if compared to V_2O_3 or VO_2 where—as discussed previously— the spectral weight is still not recovered at 6 eV [23]. This points to a reduced impact of electron correlation in the
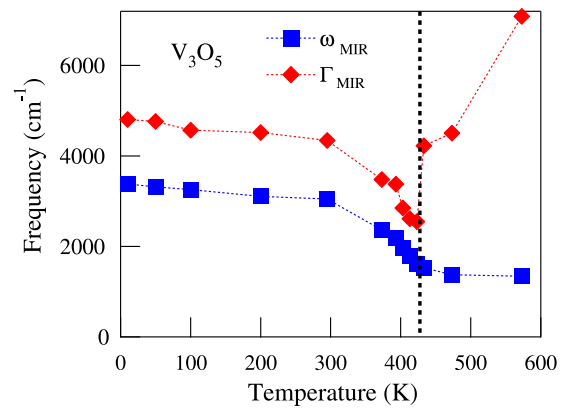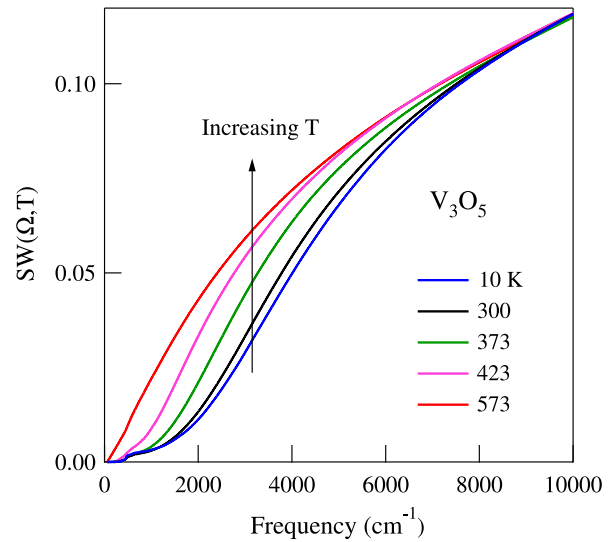
properties of V_3O_5, where the electron–lattice interaction seems to be much more important.

Optical data therefore confirm the explanation of the MIT in V_3O_5 in terms of polaron localization. In the insulating phase hole carriers are confined within the V(11) octahedra (with valence 4+), i.e. the most distorted ones. As suggested by diffraction, the V(11) octahedra are spatially ordered at low temperature, as expected for a polaronic Wigner crystal. The HF-MIR band observed in the optical spectra thus corresponds to photo-induced hopping processes of polaronic carriers from V(11) to the less distorted V^{3+} octahedra. The peak energy of HF-MIR provides an estimate for the localization energy of the polarons within the Wigner crystal. At low temperature, the three V^{3+} octahedra display different distortions, thus determining a distribution of localization energies which widens the bandwidth of HF-MIR. According to diffraction data, with increasing temperature the differences in the distortions between different octahedra reduces, thus explaining the decrease of Γ_{HF-MIR}.
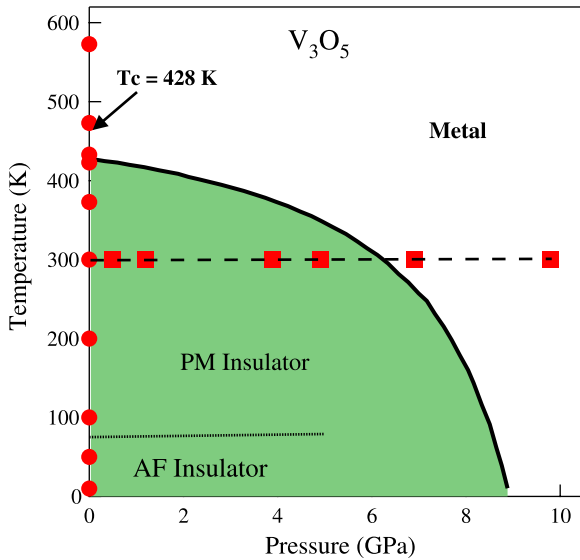
Figure 17. Pressure versus temperature phase diagram of V_3O_5 as determined in [72]. The AF order is found at ambient pressure below $T_N = 75$ K. The thick curve represents the P dependence of T_N [73]. The measurements performed in this work (versus both T and P) have been collected over the red markers shown in the figure.

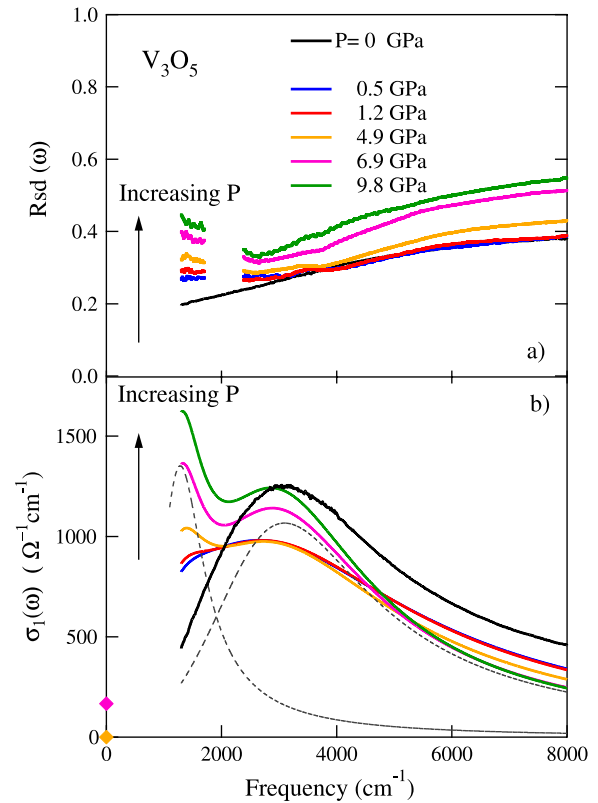**Figure 18.** (a) $R_{sd}(\omega)$ of V_3O_5 at the sample–diamond interface at room temperature for selected pressures and compared to the ambient pressure (black line) sample–diamond reflectivity. (b) Pressure-dependent optical conductivity of V_3O_5, as extracted from the LD fit. Thin dashed lines are the HF- and the LF-MIR components of the fit for $P = 9.8$ GPa data. Reprinted with permission from [70]. Copyright 2007 by the American Physical Society.

In the high temperature state, the fast exchange among V(1) lattice sites results in poor metallic conductivity. This implies diffusive motion and absence of a Drude peak in the optical conductivity. The optical transitions between V(1) and V(2) octahedra lead to the infrared absorption at LF-MIR. LF-MIR is lower in energy than HF-MIR (1000 against 3000 cm^{-1}) since the structural difference between V(1) and V(2) is lower than that between V(11) and V(12), V(21) and V(22) octahedra. According to the large Γ_{MIR} values observed at high temperature, this phase can be described in terms of disordered small polarons.

7.3. V_3O_5 versus pressure

The P–T phase diagram of V_3O_5, as determined by Sidorov et al [72], is reported in figure 17. T_{MIT} reduces as pressure is increased and vanishes at about 9 GPa, suggesting the existence of a quantum critical point for this material. At room temperature, a pressure-induced MIT occurs at about 6.3 GPa, where a discontinuity in the resistivity is found. The behaviour of T_N has been determined as a function of pressure as well [73]: only a slight increase of T_N is found at a rate of 0.82 K GPa^{-1}, up to 5 GPa.

Reflectivity measurements as a function of pressure were performed at ambient temperature. Pressure induces an enhancement of the reflectivity level over the whole measured range. The quantity

$$\frac{\Delta R}{R} = \frac{R(P) - R(P = 0.5 \text{ GPa})}{R(P = 0.5 \text{ GPa})} \qquad (13)$$

evaluated at 1600 cm^{-1} is reported in figure 19. A phenomenological sigmoid fit to the data permits us to estimate directly from the reflectivity the pressure $P_{MIT} = 6$ GPa at

which room temperature metallization occurs. This value is in very good agreement with the value determined by the pressure-dependent resistivity measurement [72]. $\Delta R/R$ has been evaluated also at other frequencies, with similar results.

The optical conductivity, as depicted in figure 18(b), has been obtained by Lorentz–Drude fitting (see section 4.2.1). The fits are consistent with a two-absorption band scenario where the two energy scales correspond to LF-MIR and HF-MIR. At variance with the temperature-dependent data where the HF-MIR band gradually shifts towards low frequency, the pressure-dependent data display coexistence of the two bands and a continuous transfer of spectral weight between them (see figure 19(b)). With increasing pressure the HF-MIR decreases, while LF-MIR increases. The sum of the two terms remains almost constant. The optical high pressure data could be fitted also by using a Drude term instead of LF-MIR. However, any reasonable fitting performed with the Drude term would lead to high values of σ_{dc}, not consistent with resistivity data [72]. Moreover, the activated behaviour of the resistivity at high pressures is further indication for negligible coherent transport, at least at room temperature.

The coexistence of the LF- and HF-MIR bands at high pressures suggests that the pressure-induced MIT relies on a different microscopic mechanism with respect to the temperature-dependent one. X-ray pressure-dependent data
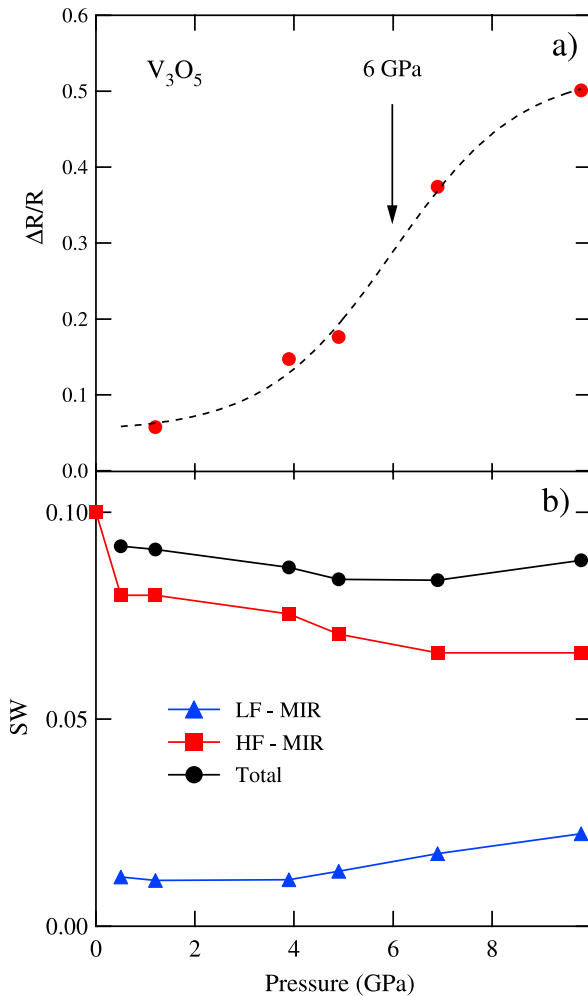
Figure 19. (a) $\Delta R/R$ at 1600 cm^{-1}. The dashed line is a phenomenological sigmoid fit to data. (b) Spectral weight of the LF-MIR, HF-MIR and total as a function of pressure from the LD fit. Reprinted with permission from [70]. Copyright 2007 by the American Physical Society.

suggest the presence of anisotropic compressibility. With pressure, the *b*-axis lattice parameter reduces more than *a* and *c*. As a consequence, the compression of the layers containing only V^{3+} octahedra is larger than that of those containing both V^{3+} and V^{4+}. Therefore, the distortion differences between tri- and tetravalent octahedra are reduced only along certain lattice directions, thus allowing the simultaneous presence of both LF-MIR and HF-MIR bands in the optical spectra.

In conclusion the charge dynamics of V_3O_5 across both the MITs induced by temperature and pressure can be explained in terms of a localization–delocalization process of lattice polarons. This suggests that the most important energy scale in V_3O_5, at variance with V_2O_3 and VO_2, is probably due to charge–lattice interaction.

8. Discussion

We finally compare the *T*- and *P*-induced MITs of the three compounds under investigation here. The focus of the present section will be on the optical spectral weight. As discussed

previously, the spectral weight permits us to probe not only the charge carriers at the Fermi level (as in a dc measurement), but also the charge which is present at low energies while not being available to transport because of a persisting tendency towards localization (e.g. *U*) also in the (bad) metallic state. Spectral weight properties of the various compounds have been extensively discussed in this review. In particular we have addressed the importance of the frequency at which the *f*-sum rule is recovered, as an indicator of the strength of electron correlation. The T^2 dependence of the spectral weight within the metallic state has been thoroughly discussed, as well, in terms of correlation (see section 5.2).

In this section we define a spectral weight-related quantity as the effective number of carriers per vanadium ion, in order to allow for a direct comparison between the three compounds of interest here. To this aim, the spectral weight was calculated at the various temperatures for each compound by integrating the optical conductivity up to the cutoff frequency which maximizes the difference between the insulating and metallic states. Such a cutoff frequency Ω_c was chosen at 10 000, 11 500 and 2400 cm^{-1} for VO_2, V_2O_3 and V_3O_5, respectively. By taking into account the electron's charge and mass, the volume of the unit cell and the number of vanadium ions per unit cell (as in equation (11)), it is possible to calculate the SW in terms of an effective number of carriers $SW_{\Omega_c} = n_{\Omega_c}/m*$. Here, $m* = m/m_0$ (m_0 being the bare electron mass) renormalizes the carrier concentration in terms of the electron mass enhancement which is expected, for example, in proximity of the Mott transition [5, 20]. Note, however, that an enhancement of the electron's mass with respect to its bare value is expected in the case of electron–phonon interaction [74], as well.

To make the comparison of $SW_{\Omega_c}(T)$ between the various compounds more straightforward, we also subtracted the value of SW_{Ω_c} found at the lowest temperatures, i.e. in the insulating state. This procedure permits us to get rid of the background due to the onset of the electronic transitions, which depends on the chosen Ω_c value. The resulting $\Delta SW_{\Omega_c}(T) = SW_{\Omega_c}(T) - SW_{\Omega_c}(0)$ is plotted in figure 20. To allow for a more easy comparison, the temperature's values have been normalized by T_{MIT} for each compound.

It is immediately noticed that the jump in SW_{Ω_c} across T_{MIT} is much more pronounced in the case of VO_2 and V_2O_3, with respect to V_3O_5. In the former cases, one observes an increase in the effective charge >0.1, whereas in the latter the enhancement is of about 0.03 only. This large difference can only partly be explained by the larger values of σ_{dc} (consistent with transport measurements), which have been observed in the correlated VO_2 and V_2O_3 compounds. One should indeed remind that for strong correlations the differences in the spectral weight extend to large frequency values, thus resulting in a further enhancement of ΔSW_{Ω_c}.

A second important point concerns the *T* dependence of ΔSW_{Ω_c} in the high temperature metallic state. It is apparent that, while for V_2O_3 the spectral weight decreases with temperature above T_{MIT}, the same behaviour is not observed for V_3O_5, where the spectral weight tends to saturation. In the case of V_2O_3, the depletion of ΔSW_{Ω_c} is associated with
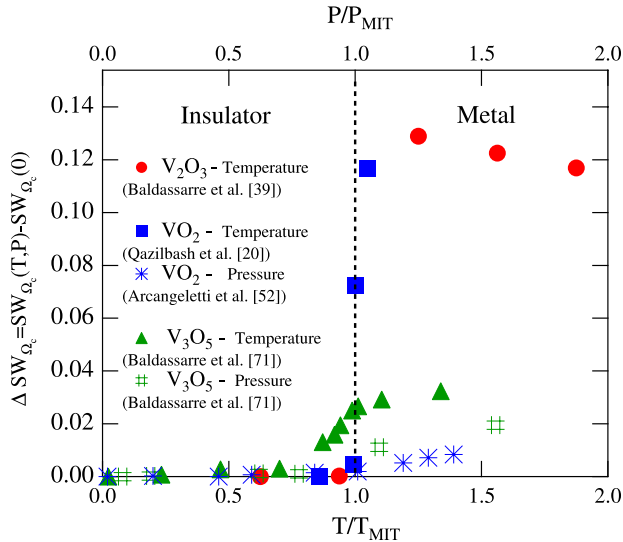
Figure 20. Plot of $\Delta SW_{\Omega_c}(T) = SW_{\Omega_c}(T) - n_{\text{eff}}(0)$ and $\Delta SW_{\Omega_c}(P) = SW_{\Omega_c}(P) - SW_{\Omega_c}(0)$ as a function of T/T_{MIT} and P/P_{MIT}, respectively (see text).

Table 1. Parameters involved in the MIT for V_2O_3, V_3O_5 and VO_2. n is the index in the formula V_nO_{2n-1}, ω_f is the frequency at which the f-sum rule is recovered (optical spectral weight conservation), T_{MIT} and P_{MIT} are the temperature (pressure) at which metallization occurs at ambient pressure (temperature), and $\Delta SW_{\Omega_c}(T)$ and $\Delta SW_{\Omega_c}(P)$ are defined in the text.

	n	ω_f (eV)	T_{MIT} (K)	$\Delta SW_{\Omega_c}(T)$	P_{MIT} (GPa)	$\Delta SW_{\Omega_c}(P)$
V_2O_3	2	>6	160	0.130	—	—
V_3O_5	3	1	428	0.032	6.3	0.0195
VO_2	∞	>6	360	0.117	10	0.008

weight is maximal) and $\Omega_c = 6000$ cm^{-1} for VO_2. Note that in the latter case we used the maximum frequency of our measurement, even though the curves between the low and high pressures do not completely merge at 6000 cm^{-1}. This implies that $\Delta SW_{\Omega_c}(P)$ for VO_2 is slightly underestimated.

We can now observe that, in the case of V_3O_5, the metallic state reached at about 10 GPa involves a gain in spectral weight which is comparable, though slightly lower, than that of the T-induced MIT. The P-induced transition is also broad, similarly to the T-dependent case. These observations are not surprising. Indeed the two transitions, while involving different microscopic mechanisms and structural rearrangements (section 7), rely nevertheless on the same physics of electron–phonon coupling and polaron formation.

On the other hand, the situation is very different for the P-induced MIT of VO_2. Here the metallic state obtained with P application involves a minor redistribution of spectral weight, i.e. less than 10% if compared to the T-induced MIT. Note also that the P-induced MIT is broad while the T-induced one is sharp. A profound difference between the two mechanisms is indeed expected since the P-induced metallic state is obtained within the monoclinic structural phase, whereas the high temperature metal is rutile. We note, however, that at the largest applied pressures the optical spectral weight still does not show signs of saturation, thus indicating that the transition is not complete.

Before concluding, we remind in table 1 of some of the most important parameters involved in the physics of the MIT of the three compounds, as discussed in this section.

9. Conclusions

Optical techniques have been therefore successfully employed in the characterization of the MIT of several vanadium oxide compounds. The main conclusions of the present work can be summarized as follows:

(i) Optics furnish important information in order to clarify the role of correlation effects. The recovery of the spectral weight at 1 eV in V_3O_5 indicates a limited role of correlation in this compound: in this case the electron–phonon mechanism seems to be much more important. On the other hand, correlation plays an extremely relevant role in V_2O_3 and VO_2 systems, where the restricted f-sum rule is violated. In the latter case the decoupling of the MIT and structural transition above 10 GPa is further evidence for the minor role played by the electron–lattice interaction.

the progressive loss of coherence of the quasiparticles, as extensively discussed in section 5.2. Data at high temperatures for VO_2 are not reported in figure 20. However, following [54], a smooth depletion of the spectral weight between 360 and 550 K is observed. The behaviour is very much like the one we observed in V_2O_3, with the important difference that, in VO_2, the quasiparticles seem to survive up to the highest temperature (dσ/dω < 0 at low frequencies, even at the highest temperatures). On the other hand, in the high temperature state of V_3O_5, the transport does not take place through a coherent mechanism, as can be deduced from the negative sign of dρ/dT. Increasing temperature above T_{MIT} promotes transport through Arrhenius-type activated behaviour of charge carriers (polarons) whose binding energy was softened across T_{MIT}.

The normalization of the temperature scale with T_{MIT} allows us to comment on the abruptness of the various MITs from an optical point of view. The difference between the correlated VO_2 and V_3O_5 is striking. The MIT in VO_2 is completed in less than 2 K, which means $\Delta T/T_{\text{MIT}}$ < 0.5%. On the other hand, the MIT of V_3O_5 as a function of temperature is broad, with $\Delta T/T_{\text{MIT}}$ exceeding 20–30%. This is further evidence of the completely different nature of the two MITs. Unfortunately, no optical data are present for V_2O_3 in close proximity to the MIT. Nevertheless, because of the abrupt resistivity jump of several orders of magnitude [43] and the strong first-order nature of the transition [32], we expect the MIT to be sharp in vanadium sesquioxide, similarly to the VO_2 case.

As a next step we try to plot the spectral weight extracted from the pressure-dependent data on the same figure 20. To this aim we normalize the pressure scale with the critical pressure P_{MIT}, similarly to what we did above with the temperature scale. We use $P_{\text{MIT}} = 6.3$ GPa for V_3O_5 and $P_{\text{MIT}} = 10$ GPa for VO_2. As cutoff frequencies we use $\Omega_c = 4500$ cm^{-1} for V_3O_5 (i.e. the frequency at which the variation of spectral

 (ii) As observed both in VO_2 and V_3O_5 the pressure-induced MITs reveal significant differences with respect to the T-induced one. This implies that phase diagrams of strongly correlated electron systems need to be fully characterized from the electrodynamic point of view in order to identify the subtle differences underlying the P- and T-induced MIT microscopic mechanisms.

(iii) Temperature-dependent optical spectra of V_2O_3 provide the clue for the understanding of its transport properties in the metallic state. The pronounced enhancement of the resistivity above 400 K is due to the downturn observed at low frequencies in the optical conductivity and the consequent pseudogap formation. This very peculiar shape of the optical conductivity is due to the simultaneous loss of coherence of the QPs at high temperatures and a lattice rearrangement.

(iv) The comparison of the optical spectra with theoretical calculations is of the greatest importance in order to evaluate the validity of the DMFT models. The early optical measurements on V_2O_3 reported in [36] helped in establishing DMFT as a powerful technique to understand the physics of strongly correlated electron systems. The results reported here, extending the temperature range of the optical measurement up to 600 K, underline the need to go beyond the single-band Hubbard model and represent a benchmark for more refined theoretical models, such as those proposed in [38] or [44].

As probably noticed by the reader, we do not present here P-dependent data on V_2O_3. This is due to the fact that V_2O_3 is already metallic at ambient T and P. As a consequence, the MIT can not be induced by applying pressure at room temperature. The exploration of the P–T phase diagram of vanadium sesquioxide is nevertheless of great interest. This may be achieved, for instance, by studying Cr-substituted V_2O_3 (which is known to become an insulator at room temperature) or by extending the optical P-dependent measurement at temperatures below 160 K.

Before concluding we remark that recent transport studies [75] on V_2O_3 microbridge patterned films display extremely peculiar behaviour that could be explained with the presence of spatially inhomogeneous MIT temperatures and phase separation. Phase separation phenomena are indeed known to occur in several strongly correlated electron systems [76]. This phenomenon is likely at the origin of CMR in manganites, while the relevance of stripe ordering phenomena in HTS is far from being understood. The study of the MIT in vanadium oxide materials also calls for a careful investigation of eventual spatial inhomogeneities, and possibly to the use of spatially resolved probes such as those employed in [20].

Acknowledgments

References

[1] Bloch F 1929 *Z. Phys.* **57** 545
[2] Bethe H 1928 *Ann. Phys.* **87** 55
[3] de Boer J H and Verwey E J W 1937 *Proc. R. Soc.* A **49** 59
[4] Grüner G 1988 *Rev. Mod. Phys.* **60** 11299
[5] Imada M, Fujimori A and Tokura Y 1998 *Rev. Mod. Phys.* **70** 1039
[6] Damascelli A, Hussain Z and Shen Z X 2003 *Rev. Mod. Phys.* **75** 472
[7] Kabanov V V, Demsar J, Podobnik B and Mihailovic D 1999 *Phys. Rev. B* **59** 1497
[8] Georges A, Kotliar G, Krauth W and Rozenberg M J 1996 *Rev. Mod. Phys.* **68** 13
[9] Magneli A 1948 *Acta Chem. Scand.* **2** 501
[10] Schwingenschlögl U and Eyert V 2004 *Ann. Phys., Lpz.* **13** 475
[11] Hubbard J 1963 *Proc. R. Soc.* A **276** 238
[12] Ong N P 1990 *Physical Properties of High Temperature Superconductors* ed D M Ginsberg (Singapore: World Scientific)
[13] Kotliar G, Savrasov S Y, Haule K, Oudovenko V S, Parcollet O and Marianetti C A 2006 *Rev. Mod. Phys.* **78** 865
[14] Anisimov V, Poteryaev A, Korotin M, Anokhin A and Kotliar G 1997 *J. Phys.: Condens. Matter* **9** 7359
[15] Sarma D D, Krishnakumar S R, Weschke E, Schüssler-Langeheine C, Mazumdar C, Kilian L, Kaindl G, Mamiya K, Fujimori S I and Fujimori A 2003 *Phys. Rev. B* **67** 155112
[16] Rodolakis F *et al* 2009 *Phys. Rev. Lett.* **102** 066805
[17] Dressel M and Grüner G 2002 *Electrodynamics of Solids* (Cambridge: Cambridge University Press)
[18] Wooten F 1972 *Optical Properties of Solids* (New York: Academic)
[19] Basov D N and Timusk T 2005 *Rev. Mod. Phys.* **77** 721
[20] Qazilbash M M *et al* 2007 *Science* **318** 1750
[21] Ortolani M, Calvani P and Lupi S 2005 *Phys. Rev. Lett.* **94** 067002
[22] Toschi A, Capone M, Ortolani M, Calvani P, Lupi S and Castellani C 2005 *Phys. Rev. Lett.* **95** 097002
[23] Qazilbash M M, Schafgans A A, Burch K S, Yun S J, Chae B G, Kim B J, Kim H T and Basov D N 2008 *Phys. Rev. B* **77** 115121
[24] Lupi S, Nucara A, Perucchi A, Calvani P, Ortolani M, Quaroni L and Kiskinova M 2007 *J. Opt. Soc. Am. B* **24** 959
[25] Perucchi A, Baldassarre L, Arcangeletti E, Di Castro D, Postorino P and Lupi S 2008 *Infrared Phys. Technol.* **51** 440
[26] Dore P *et al* 1998 *Appl. Opt.* **37** 5731
[27] Pashkin A, Dressel M and Kuntscher C A 2006 *Phys. Rev. B* **74** 165118
[28] Lavagnini M, Sacchetti A, Degiorgi L, Arcangeletti E, Baldassarre L, Postorino P, Lupi S, Perucchi A, Shin K Y and Fisher I R 2007 *Phys. Rev. B* **77** 165132
[29] Lavagnini M, Sacchetti A, Marini C, Sopracase R, Perucchi A, Postorino P, Lupi S, Chu J H, Fisher I R and Degiorgi L 2009 *Phys. Rev. B* **79** 075117
[30] McWhan D B, Rice T M and Remeika J P 1969 *Phys. Rev. Lett.* **23** 1384
[31] Jayaraman A, McWhan D B, Remeika J P and Dernier P D 1970 *Phys. Rev. B* **2** 3751
[32] Limelette P, Georges A, Jerome D, Wzietek P, Metcalf P and Honig J M 2003 *Science* **302** 89
[33] Frenkel A I, Pease D M, Budnick J I, Metcalf P, Stern E A, Shanthakumar P and Huang T 2006 *Phys. Rev. Lett.* **97** 195502
[34] Robinson W R 1975 *Acta Crystallogr.* **31** 1153
[35] McWhan D B and Remeika J P 1970 *Phys. Rev. B* **2** 3734
[36] Rozenberg M J, Kotliar G, Kajueter H, Thomas G A, Rapkine D H, Honig J M and Metcalf P 1995 *Phys. Rev. Lett.* **75** 105
[37] Keller G, Held K, Eyert V, Volhardt D and Anisimov V I 2004 *Phys. Rev. B* **70** 205116

[38] Baldassarre L *et al* 2008 *Phys. Rev. B* **77** 113107
[39] Yang J, Hwang J, Timusk T, Sefat A S and Greedan J E 2006 *Phys. Rev. B* **73** 195125
[40] Held K, Keller G, Eyert V, Vollhardt D and Anisimov V I 2001 *Phys. Rev. Lett.* **86** 5345
[41] Castellani C, Natoli C R and Ranninger J 1978 *Phys. Rev. B* **18** 4945
    Castellani C, Natoli C R and Ranninger J 1978 *Phys. Rev. B* **18** 4967
    Castellani C, Natoli C R and Ranninger J 1978 *Phys. Rev. B* **18** 5001
[42] Park J H, Tjeng L H, Tanaka A, Allen J W, Chen C T, Metcalf P, Honig J M, de Groot F M and Sawatzky G A 2000 *Phys. Rev. B* **61** 11506
[43] Kuwamoto H, Honig J M and Appel J 1980 *Phys. Rev. B* **22** 2626
[44] Tomczak J M and Biermann S 2009 *J. Phys.: Condens. Matter* **21** 064209
[45] Poteryaev A I, Tomczak J M, Biermann S, Georges A, Lichtenstein A I, Rubtsov A N, Saha-Dasgupta T and Andersen O K 2007 *Phys. Rev. B* **76** 085127
[46] Metcalf P A, Guha S, Gonzales L P, Barnes J O, Slamovich E B and Honig J M 2007 *Thin Solid Films* **515** 3421
[47] Morin F J 1959 *Phys. Rev. Lett.* **3** 34
[48] Cavalleri A, Dekorsy Th, Chong H H W, Kieffer J C and Schoenlein R W 2004 *Phys. Rev. B* **70** 161102
[49] Hilton D J, Prasankumar R P, Fourmaux S, Cavalleri A, Brassard B, El Khakani M A, Kieffer J C, Taylor A J and Averitt R D 2007 *Phys. Rev. Lett.* **99** 226401
[50] Nakajima N, Takubo N, Hiroi Z, Ueda Y and Suemoto T 2008 *Appl. Phys. Lett.* **92** 011907
[51] Arcangeletti E, Baldassarre L, Di Castro D, Lupi S, Malavasi L, Marini C, Perucchi A and Postorino P 2007 *Phys. Rev. Lett.* **98** 196406
[52] Marini C *et al* 2008 *Phys. Rev. B* **77** 235111
[53] Biermann S, Poteryaev A, Lichtenstein A I and Georges A 2005 *Phys. Rev. Lett.* **94** 026404
[54] Qazilbash M M, Burch K S, Whisler D, Shrekenhamer D, Chae B G, Kim H T and Basov D N 2006 *Phys. Rev. B* **74** 205118
[55] Barker A S, Verleur H W and Guggenheim H J 1996 *Phys. Rev. Lett.* **17** 1286
[56] Verleur H W, Barker A S and Berglund C N 1968 *Phys. Rev.* **172** 788
[57] Okazaki K, Sugai S, Muraoka Y and Hiroi Z 2006 *Phys. Rev. B* **73** 165116
[58] Choi H S, Ahn J S, Jung J H, Noh T W and Kim D H 1996 *Phys. Rev. B* **54** 4621
[59] Tomczak J M and Biermann S 2008 arXiv:0807.4044v1 [cond-mat] unpublished
[60] Marezio M, McWhan D B, Remeika J P and Dernier P D 1972 *Phys. Rev. B* **5** 25411
[61] Pouget J P, Launois H, Rice T M, Dernier P, Gossard A, Villeneuve G and Hagenmuller P 1974 *Phys. Rev. B* **10** 1801
[62] Rice T M, Launois H and Pouget J P 1994 *Phys. Rev. Lett.* **73** 3042
[63] Baldini M *et al* 2007 unpublished
[64] Terukov E I and Chudnovskii F A 1974 *Fiz. Tekh. Poluprovodn.* **8** 1266
[65] Chudnovskii F A, Terukov E I and Khomskii D I 1978 *Solid State Commun.* **25** 537
[66] Hong S H and Asbrink S 1982 *Acta Crystallogr. B* **38** 713
[67] Asbrink A 1980 *Acta Crystallogr. B* **36** 1332
[68] Verwey E J W 1939 *Nature* **144** 327
[69] Andersson G 1954 *Acta Chem. Scand.* **8** 1599
[70] Baldassarre L, Perucchi A, Arcangeletti E, Nicoletti D, Di Castro D, Postorino P, Sidorov V A and Lupi S 2007 *Phys. Rev. B* **75** 245108
[71] Gasparov L V, Tanner D B, Romero D B, Berger H, Margaritondo G and Forró L 2000 *Phys. Rev. B* **62** 7939
[72] Sidorov V A, Waskowska A and Badurski D 2003 *Solid State Commun.* **125** 359
[73] Sidorov V A *et al* 2007 unpublished
[74] Calvani P 2001 *Riv. Nuovo Cimento* **24** 1
[75] Grygiel C, Pautrat A, Sheets W C, Prellier W, Mercey B and Méchin L 2008 *J. Phys.: Condens. Matter* **20** 472205
[76] Dagotto E 2005 *Science* **309** 257